Inorganic Chemistry

pubs.acs.org/IC Article

Inducing Ferrimagnetic Exchange in 1D-FeSe₂ Chains Using Heteroleptic Amine Complexes: [Fe(en)(tren)][FeSe₂]₂

Eranga H. Gamage, Saeed Kamali, Govind Sasi Kumar, Judith K. Clark, Yongbin Lee, Yao Abusa, Philip Yox, Liqin Ke, Michael Shatruk, and Kirill Kovnir*



Cite This: Inorg. Chem. 2024, 63, 2443-2453



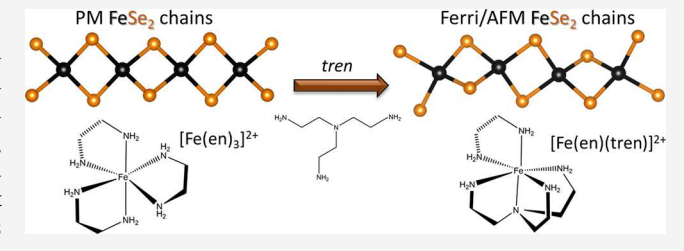
ACCESS I

III Metrics & More

Article Recommendations

sı Supporting Information

ABSTRACT: [Fe(en)(tren)][FeSe₂]₂ (*en* = ethylenediamine, $C_2H_8N_2$, *tren* = tris(2-aminoethyl)amine, $C_6H_{18}N_4$) has been synthesized by a mixed-ligand solvothermal method. Its crystal structure contains heteroleptic [Fe(en)(tren)]²⁺ complexes with distorted octahedral coordination, incorporated between 1D-FeSe₂ chains composed of edge—sharing FeSe₄ tetrahedra. The twisted octahedral coordination environment of the Fe—amine complex leads to partial dimerization of Fe—Fe distances in the FeSe₂ chains so that the FeSe₄ polyhedra deviate strongly from the regular



tetrahedral geometry. ⁵⁷Fe Mössbauer spectroscopy reveals oxidation states of +3 for the Fe^{chain} atoms and +2 for the Fe^{complex} atoms. The close proximity of Fe atoms in the chains promotes ferromagnetic nearest neighbor interactions, as indicated by a positive Weiss constant, $\theta = +53.8(6)$ K, derived from the Curie–Weiss fitting. Magnetometry and heat capacity reveal two consecutive magnetic transitions below 10 K. DFT calculations suggest that the ordering observed at 4 K is due to antiferromagnetic *intra*chain interactions in the 1D-FeSe₂ chains. The combination of two different ligands creates an asymmetric coordination environment that induces changes in the structure of the Fe–Se fragments. This synthetic strategy opens new ways to explore the effects of ligand field strength on the structure of both Fe-amine complexes and surrounding Fe–Se chains.

INTRODUCTION

Tuning of superconducting and magnetic properties in Febased pnictides and chalcogenides has been one of the most widely explored fields of solid-state chemistry and condensed matter physics in the past few decades. Since the remarkable discovery of superconductivity in cuprates, 1,2 the next most notable breakthrough in this field was the observation of superconductivity in tetragonal layers of Fe pnictides and chalcogenides.^{3,4} Those discoveries inspired the studies of organic-inorganic hybrid compounds containing tetrahedral FeQ_4 building blocks (Q = S, Se). Even though most of these compounds act as antiferromagnetic (AFM) insulators, they are proposed as model systems to bridge the gap between superconducting cuprates and Fe pnictides and chalcogenides due to the similarities in their electronic and crystal structures. The alkalizelenoferrates, $AFeQ_2$ (A = alkali metal), which contain one-dimensional (1D) chains of edge-sharing FeQ4 tetrahedra, were reported to exhibit strong magnetic exchange interactions between Fe atoms. $^{5-10}$ The studies of AFe Q_2 compounds proved that variation in the size of the cation located between the FeQ2 chains can impact the magnetic properties.

The intercalation chemistry of larger organic-inorganic spacer molecules, such as ammonia, hydroxides, and linear diamines, in the interlayer space of FeQ superconductors has been thoroughly investigated. In certain instances,

intercalation led to the occurrence of vacancies in the layers and loss of superconductivity, giving rise to moderate AFM nearest-neighbor interactions between Fe atoms in adjacent tetrahedra. The same structural design was applied to 1D Fe chalcogenide chains to study the impact of host—guest interactions on the magnetic properties due to structural rearrangements. Distortion in the FeSe₂ chains was found to correlate with the type and strength of the *intra*chain magnetic interactions. Multidentate amines have been used as chelating agents to form bulky Fe—amine spacer complexes and induce a distortion in the FeSe₂ chains. Fe atoms in the amine complexes usually prefer local octahedral coordination geometry provided by one or more ligands, depending on the ligand's denticity.

Previous studies have reported the use of bidentate ethylenediamine (en) to form isolated or covalently bound Fe-en complexes residing between FeSe₂ chains. In [Fe(en)₂]-[FeSe₂]₂,²¹ Fe(en)₂Se₂ fragments connect to two adjacent tetrahedral FeSe₂ chains to form a 3D AFM covalent network

Received: October 2, 2023
Revised: December 22, 2023
Accepted: December 27, 2023
Published: January 22, 2024





with strong nearest neighbor interactions. Several compounds with isolated $[Fe(en)_3]^{2+}$ complexes between tetrahedral chains stabilized by ionic and hydrogen bonding interactions have been reported by Johrendt and co-workers. For example, $[Fe(en)_3][FeSe_2]_2$ shows weak *intra*chain AFM coupling due to longer Fe—Fe bond distances. A combination of $[Fe(en)_3]^{2+}$ cations together with Cl^- anions in the interchain space results in $[Fe(en)_3]_3(FeSe_2)_4Cl_2$, with strong *intra*chain and weak *inter*chain AFM exchange interactions that lead to a spin glass behavior due to magnetic frustration. Covalent modification of 1D $[Fe_5Se_9]$ chains by chiral $[As_3Se_2]$ -Se linkers effectively induces short-range ordering in chains at around 50 K.

Tris(2-aminoethyl)amine (tren) is a tetradentate chelating ligand with C_3 symmetry. Although tren usually serves as a tetramine, it may behave as a tridentate ligand, in which case the uncoordinated primary amine could serve as a cross-linking agent. 27,28 Many tren-based tripod ligands have been employed to design Fe(II) spin crossover complexes. ^{29,30} Because of its high affinity toward 3d transition metal (TM) cations, tren is also popular in the main group thiometallate chemistry to generate $[TM(amine)_x]^{2+}$ complexes. Moreover, in polymer synthesis, derivatives of tren have been extensively applied as catalysts for copper-based atom transfer radical polymerization.³⁴ Apart from this, tren was utilized in the form of cis- $[Fe(tren)Se_2]^{2+}$ complexes in the structure of [Fe(tren)]-[FeSe₂]₂, where the tetradentate amine leaves Fe^{complex} coordinatively unsaturated, forcing it to bind with two Se atoms of the same FeSe2 chain. This design led to strong intrachain ferromagnetic (FM) nearest-neighbor interactions due to reduced Fe-Fe bond distances in the chains and 3D AFM ordering of the FM chains.

In addition to the aforementioned tetrahedral FeSe₂ chain compounds with Fe-en or Fe-tren complexes, a similar chain compound [Fe(dien)₂][FeSe₂]₂, with significantly suppressed complex-chain interactions, has been synthesized using the bidentate ligand diethylenetriamine (dien).20 Importantly, all of these chain compounds contain only homoleptic Fe-amine complexes. To the best of our knowledge, no FeSe₂ chain compound with a heteroleptic Fe-amine complex has been reported to date. Incorporation of such heteroleptic complexes, with an asymmetric coordination environment between FeSe₂ chains, can lead to substantially different crystal packing motifs and, consequently, novel magnetic behaviors. Here we report the design, synthesis, magnetism, ⁵⁷Fe Mössbauer spectroscopic, heat capacity studies, and DFT calculations of a novel compound, [Fe(en)(tren)][FeSe2]2, where neutral en and tren ligands together complete the octahedral coordination environment of the Fe-amine complex. This compound can be identified as the groundwork toward the incorporation of spin crossover complexes into FeSe2 chain compounds to obtain novel materials with interesting magnetic and photochemical properties.

■ EXPERIMENTAL SECTION

Synthesis. Single phase samples of [Fe(en)(tren)][FeSe₂]₂ were synthesized by a low-temperature solvothermal route employing a mixed solvent system containing equal volumes of ethylenediamine (99%, Alfa Aesar) and tris(2-aminoethyl) amine (Alfa Aesar, 97%). A 46 mL Teflon lined stainless steel autoclave was loaded with 1 mmol of iron powder (<10 μ m, Alfa Aesar, 99.5%), 1.33 mmol of selenium powder (Sigma-Aldrich, >99.5%), and 2 mmol of ammonium chloride (Fisher Scientific, 99%) followed by the addition of 10 mL of *en* (150 mmol) and 10 mL of *tren* (67 mmol) ligands up to a filling fraction of

43%. Then the autoclave was tightly closed and placed in a furnace at $200~^{\circ}\text{C}$ for 4 days. After that, the sample was taken out of the furnace and naturally cooled to room temperature. The contents were filtered with aliquots of 100% ethanol and the black thin needle-like crystals (Figure 1 inset) recovered were stored in an argon filled glovebox to

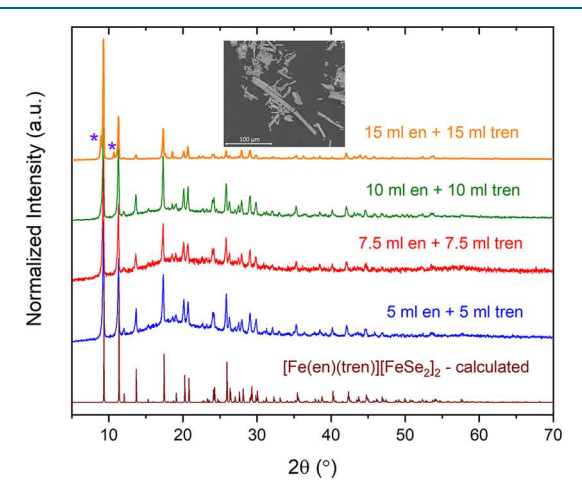


Figure 1. Powder X-ray diffraction (PXRD, λ = 1.54185 Å) patterns of the products obtained from the reaction of 3Fe + 4Se + NH₄Cl at 200 °C by varying *en* and *tren* volumes, i.e., filling fractions of 46 mL autoclave. Inset: Back scattered electron image of thin needle—like crystals of [Fe(en)(tren)][FeSe₂]₂. Peaks of the admixture phase [Fe(tren)][FeSe₂]₂ are indicated with asterisks (*). The calculated pattern of the title compound is provided at the bottom.

prevent oxidation or degradation. When stored under ambient conditions, the crystals turn reddish-brown over the course of a few hours.

To test different filling fractions, starting materials were scaled up with increasing solvent fractions to keep their concentrations constant (Figure 1). When the synthesis was carried out in 23 mL liners with a 65% filling fraction, after a slow cooling process over 2 weeks, better quality crystals with no impurities were obtained to perform single crystal X-ray diffraction. Changing the volume ratio of solvents *en: tren* from 1:1 to 1:2 or 3:4 resulted in the formation of two previously reported compounds, $[Fe(en)_2][FeSe_2]_2$ and $[Fe(tren)][FeSe_2]_2$, latter being the major phase. 20,21 Using lower filling fractions yields less crystalline products with unidentified admixtures, while prolonged thermal treatment favors the formation of the $[Fe(tren)][FeSe_2]_2$ compound as the only product.

Characterization. PXRD patterns of the synthesized products were obtained on a Rigaku 600 miniflex benchtop diffractometer using $\text{Cu-}K_{\alpha}$ radiation ($\lambda=1.54185\,\text{ Å}$) and a $\text{Ni-}K_{\beta}$ filter. Fluorescence reduction was applied to minimize the high background due to the fluorescence of Fe atoms and grease was used to sprinkle fine powder onto sample holder plates. *In-situ* synchrotron PXRD studies were conducted at the beamline 17-BM-B ($\lambda=0.24075\,\text{Å}$), Advanced Photon Source, Argonne National Laboratory using the setup mimicking solvothermal conditions described elsewhere. ²³

Preliminary single crystal X-ray diffraction data of the needle-like crystals was obtained on a Bruker Venture D8 diffractometer employing Mo- K_{α} radiation ($\lambda=0.71073$ Å) and a Photon100 CMOS detector. Crystals were mounted on a cryoloop and placed on the goniometer followed by cooling to 100 K under a dry N₂ flow. A high-resolution synchrotron single crystal X-ray diffraction experiment was performed at the 15-ID-B beamline ($\lambda=0.41328$ Å) of the Advanced Photon Source, Argonne National Laboratory at 100 K. Data analysis and crystal structure solution were performed using APEX3 and SHELX crystallographic software packages. \$\frac{35,36}{5}\$ An empirical adsorption correction (multiscan routine) was applied.

Energy dispersive X-ray spectroscopy (EDX) experiment was conducted on a FEI Quanta 250 field emission-SEM spectrometer

with EDX detection (Oxford X-Max 80) to estimate the elemental composition of the needle-like crystals. An electron beam of 15 keV energy and a working distance of 10 mm were employed for data collection. The composition of the crystals normalized to 4Se atoms was estimated to be $Fe_{3.0(1)}Se_4$. CHN organic component analysis conducted on a Thermo FlashSmart 2000 CHNS/O Combustion Elemental Analyzer using several milligrams of finely powdered dry sample yielded an organic chemical composition of $C_{9.1(7)}N_{6.1(4)}H_{28(1)}$ which matches the composition derived from single crystal X-ray diffraction, $Fe_3Se_4C_9N_6H_{27}$.

Magnetic measurements were conducted on a magnetic property measurement system MPMS-XL (Quantum Design) equipped with a superconducting quantum interference device (SQUID). Finely ground powder (5.6 mg) was used to study the temperature dependence of field-cooled (FC) and zero-field-cooled (ZFC) magnetization in a 1000 Oe applied field. The diamagnetic contribution from the sample holder and the intrinsic diamagnetic interactions (χ_{dm}) of the sample were subtracted from the measured total magnetic susceptibility (χ_{meas}) to obtain the net paramagnetic susceptibility (χ_{pm}). Curie-Weiss fit was performed for different temperature ranges, N to 300 K, where N = 50, 100, 125, 150, 175, and 200 K. The obtained fit parameters, Curie constant and Weiss temperature, depend on the chosen temperature range for N < 175 Kbut remain unchanged within fit uncertainty for $N \ge 175$ K. The temperature range of 175-300 K was selected as the final fit. The temperature-independent contribution, χ_0 , was omitted from the fit because the standard deviation obtained for the parameter was higher than the absolute value. Isothermal magnetization was investigated in a varying field of 0-7 T at 1.8 K. To check for the reproducibility of the magnetic behavior, a new sample of the title compound was synthesized later by a different researcher in our group using the reported methodology. The magnetic properties of the new sample were measured in 1000 Oe and 3 T applied field. The former measurement reproduced the original data (Figure S3).

⁵⁷Fe Mössbauer spectroscopy was used to investigate the oxidation state and magnetic properties of the $[Fe(en)(tren)][FeSe_2]_2$ compounds. The measurements were performed at 6, 50, and 293 K using an MS4 spectrometer operating in the constant acceleration mode in transmission geometry and a 50 mCi ⁵⁷Co in Rh held at room temperature as a source. For low-temperature measurements, a Janis closed-cycle refrigerator was used. All centroid shifts, δ, are given with respect to metallic α-iron measured at RT. All spectra were least-squares fitted by a Lorentzian analysis using Recoil software³⁷ to extract hyperfine parameters, which are δ, quadrupole splitting/quadrupole shift $(\Delta E_Q/\varepsilon)$, magnetic hyperfine field (B_{hf}) , fullwidth at half—maximum (Γ) , and intensity (I).

Heat capacity was measured on a part of a pellet (maximum dimension 3 mm) pressed using a 6 mm die on a hydraulic press applying a force of 5t under ambient temperature. The pellet was attached to a sample puck with the help of an Apiezon N grease. Heat capacity measurements were performed on a quantum design physical property measurement system (PPMS) from 1.8 to 100 K under zero and 1 T applied field. Addenda measurements were taken under both fields to account for the contributions of grease and the holder. Under higher applied fields of 4 and 7 T, the pellet was blown away from the puck probably due to magnetostriction. Attempts to use heavier pellets and more grease were unsuccessful. Good quality data from 1.8 to 100 K were obtained only under 0 and 1 T applied fields.

FTIR spectra of the solid samples were obtained by the KBr pellet method on a Bruker Tensor 37 spectrometer. KBr and the sample were ground together and loaded into the die under inert conditions, but pressed using a mechanical press under ambient conditions. Steps were taken to conduct the measurement fast enough with a minimum exposure to atmospheric conditions.

The first-principles calculations were performed using the projected augmented-wave method³⁸ as implemented in the Vienna *ab initio* simulation package (VASP).^{39,40} For exchange-correlation functional, we employed the Perdew, Burke, and Ernzerhof (PBE)⁴¹ parametrization in the generalized gradient approximation (GGA). A plane wave cutoff of 350 eV and the 9×12×6 *k*-point mesh grid were

employed. Due to the large unit cell size with many atoms present in the compound, [Fe(en)(tren)]²⁺ complexes were replaced with Ba²⁺ cations to simplify the structure and make the calculations manageable. Hence, magnetic interactions were analyzed in the Fe-Se chains of the hypothetical structure of Ba₄[FeSe₂]₈. Exchange constants were calculated using an in-house ab initio tight binding (TB) framework.⁴² Realistic TB Hamiltonians were constructed via the maximally localized Wannier functions (MLWFs) method⁴³ as implemented in Wannier9044 through a postprocedure using the output of the self-consistent DFT calculations. 45,46 The details of our methods and application can be found in ref 42. We constructed the TB Hamiltonian using 252 MLWFs, which correspond to s-, p- and dtype orbitals for all Fe, Se, and Ba atoms in the unit cell. A real-space Hamiltonian H(R) with dimensions 252×252 was constructed to accurately represent the band structures in the energy window of interest.

RESULTS AND DISCUSSION

Synthesis. To understand the mechanism of formation and decomposition of [Fe(tren)][FeSe₂]₂, in situ PXRD experiments were conducted on finely ground powders placed in capillaries injected with solvent under 500 psi of argon pressure. When the solvent mixture (en + tren) was injected into the finely ground powders containing Fe + Se + NH₄Cl, Fe(en)₃Cl₂ formed immediately and remained until 225 °C (Figure 2). At ~170 °C, the formation of binary FeSe₂ was observed. Traces of the target phase, [Fe(en)(tren)][FeSe₂]₂, appear when the temperature reaches ~200 °C. From 200—320 °C, the changing intensities of the peaks indicate how [Fe(en)(tren)][FeSe₂]₂ grows to become the major phase while FeSe₂ becomes the minor phase. This result demonstrates the rearrangement of FeSe₆ octahedra in ferroselite into

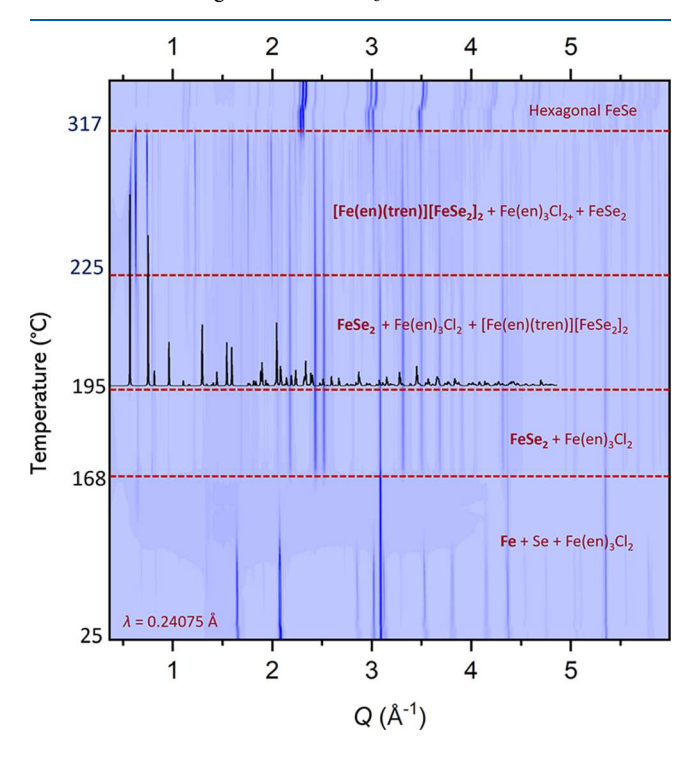


Figure 2. Contour plot of the *in situ* reaction of Fe + Se + NH $_4$ Cl in a mixture of ethylenediamine and tris(2-aminoethyl)amine in an open capillary pressurized with 500 psi of argon. Phase composition of each region is indicated with the main phase highlighted in **bold**. A reference calculated room-temperature PXRD pattern for the title compound is shown in black. All of the other reference PXRD patterns are provided in Figure S1.

FeSe $_4$ tetrahedra in [Fe(en)(tren)][FeSe $_2$] $_2$ with the incorporation of [Fe(en)(tren)] $^{2+}$ complexes between FeSe $_2$ chains. When the temperature increases above 300 °C, the [Fe(en)(tren)][FeSe $_2$] $_2$ structure collapses to form hexagonal FeSe.

Crystal Structure. [Fe(en)(tren)][FeSe₂]₂ crystallizes in an orthorhombic space group *Pnma* (No. 62). The crystal structure was determined from a synchrotron single crystal diffraction data set (Table 1). Several C, N, and H light atoms

Table 1. Single Crystal Data Collection and Structure Refinement Parameters for [Fe(en)(tren)][FeSe₂]₂; Further Details of the Crystal Structure Determination Maybe Obtained by Quoting the CCDC Number 2202574

source	synchrotron
CCDC number	2202574
temperature (K)	100(2)
λ (Å)	0.41328
crystal system	Orthorhombic
space group	Pnma (No. 62)
a (Å)	11.5664(5)
b (Å)	8.5287(5)
c (Å)	18.9407(2)
V (Å ³)	1868.43(2)
Z	4
formula weight (g mol ⁻¹)	689.74
$ ho_{ m calc}$ (g cm $^{-3}$)	2.45
$\mu \text{ (mm}^{-1})$	2.30
data/parameters	1646/134
R_1/wR_2	0.034/0.081
GOF	0.898
diff. peak/hole (e ų)	0.88/-0.65

are located at split sites due to the mirror planes bisecting the amine ligands. Lowering of the symmetry to the monoclinic $P2_1/n$ space group to remove those mirror planes did not resolve the disorder associated with the Fe-ligand complex. Crystal structure solution in an orthorhombic unit cell converges to a final R_1 value of 0.034. Experimental and calculated powder X-ray diffraction patterns are in good agreement (Figure 3b). Crystal structures with the atomic displacement parameters as ellipsoids are given in Figure S2.

Similar to the organic—inorganic hybrid chain compounds discussed above, [Fe(en)(tren)][FeSe₂]₂ consists of one-dimensional chains of edge-sharing FeSe₄ tetrahedra propagating along the [100] direction (Figure 3a). The Fe-amine interstitial species is the isolated [Fe(en)(tren)]²⁺ complex with a distorted octahedral geometry. The Fe1 and Fe2 atoms reside in the chains while the Fe3 atoms belong to the amine complex. Two distinctly different Fe–Fe distances are observed in the FeSe₂ chains, at 2.899(2) and 2.971(2) Å (Figure 3c). As a result, the Fe–Fe–Fe bond angles along the chain deviate substantially from linearity, down to 169.1 and 163.5° (Figure 3c). The formula unit contains two symmetry-equivalent Se2 atoms and two N5–C5–C6–N4 chelate rings generated by the mirror operation in the *ac* plane (Figure 3d).

The [Fe(en)(tren)]²⁺ complex exhibits a noticeably distorted octahedral coordination. The chelate rings of the ligands bound to Fe3 atoms are arranged perpendicular to each other to minimize steric repulsion (Figure 3d,e). The N1, N2, N3, and N4 atoms lie on the same *ac*-plane but bending of the Fe–N bonds along the *c*-axis results in a reduced N5–Fe3–N5

angle of 152.2° (Figure 3d). As a result, there are obvious long and short Fe-N bond distances in the complex, within ~0.115 Å difference. Nevertheless, the average Fe-N bond distance of 2.22(6) Å is typical for the high spin Fe²⁺ complexes.⁴⁷ Since the mirror plane runs through the [Fe(en)(tren)]²⁺ complex on the *ac* plane, certain positions of C and N atoms are split; they have been refined with a 50% site occupancy. Visualizing the structure along the a-axis clearly reveals the separation of the [Fe(en)(tren)]²⁺ complexes from the surrounding chains (Figure 3e).

The degree of distortion in the FeSe2 chains in $[Fe(en)(tren)][FeSe_2]_2$ is similar to that in [Fe(tren)]-[FeSe₂]₂. ²⁰ Both structures have two different Fe-Fe bond distances in the chains, with one distance ~0.07 Å longer than the other (Table 2). However, the Se-Fe-Se angles in the FeSe₄ tetrahedra are more acute and the Fe-Fe bond distances are shorter in [Fe(tren)][FeSe2]2 compared to those in [Fe(en)(tren)][FeSe2]2, due to the heavily distorted cis-Fe(tren)Se₂ motifs in the former. The shorter Fe-Fe bond distances and smaller Fe-Fe-Fe angles in the chains can certainly be recognized as factors that promote FM exchange between Fe^{chain} atoms. When juxtaposed with other chain compounds containing isolated homoleptic Fe-amine complexes, $[Fe(en)_3][FeSe_2]_2^{22}$ and $[Fe(dien)_2][FeSe_2]_2^{20}$ the [Fe(en)(tren)][FeSe₂]₂ structure can be identified as the chain compound with the most contracted FeSe4 tetrahedra. However, when interstitial anions come into the picture, as in [Fe(en)₃]₃(FeSe₂)₄Cl₂, ²³ the tetrahedra tend to be slightly more contracted than in the case of [Fe(en)(tren)][FeSe₂]₂. Overall, it is evident that the incorporation of the asymmetric heteroleptic Fe-amine complex results in a higher degree of bending in the FeSe2 chains compared to the structures with more symmetric homoleptic tris- and bis-amine complexes of ligands such as en and dien.

According to electron counting, Fe^{chain} atoms acquire a +3 charge giving a -2 charge to the $[FeSe_2]_2$ 1D chain, which in turn is compensated by the $Fe^{complex}$ atoms of +2 charge: $[Fe^{2+}(en)(tren)][Fe^{3+}Se^{2-}]_2$. Bond valence sum $(BVS)^{48}$ calculations yielded a charge of +3.04 on both Fe1 and Fe2 atoms in the chains. Since the $[Fe(en)(tren)]^{2+}$ complex makes no covalent connections with the $FeSe_2$ chains, the crystal structure with two basic subunits is supported by noncovalent interactions, i.e., ionic and hydrogen bonding interactions. A network of N-H···Se hydrogen bonds of 2.674-2.775 Å distance and $122.2-126.9^\circ$ angles associated with the NH₂ groups of both amine ligands is an important factor for the stability of the structure.

FTIR Spectroscopy. The FTIR spectrum of [Fe(en)(tren)][FeSe₂]₂ is complicated due to the presence of many absorption bands characteristic of different vibrational modes of the -NH₂ and -CH₂ groups in both *en* and *tren* ligands. It is difficult to distinguish between the bands of the distinct ligands because of significant spectral overlaps. We compare the spectrum of [Fe(en)(tren)][FeSe₂]₂ with the heteroleptic [Fe(en)(tren)]²⁺ cation to the spectra of [Fe(en)₃]₃(FeSe₂)₄Cl₂ with the homoleptic [Fe(en)₃]²⁺ cation and [Fe(tren)][FeSe₂]₂ with the cation [Fe(tren)]²⁺ that contains a single *tren* ligand (Figure 4). For [Fe(tren)]-[FeSe₂]₂, the bands are not well-resolved, and the spectrum is noisy, which could be due to the presence of trace amounts of Fe(tren)Cl₂ impurity. Band assignment was performed by referring to the spectra of several reported compounds containing multidentate amine ligands.

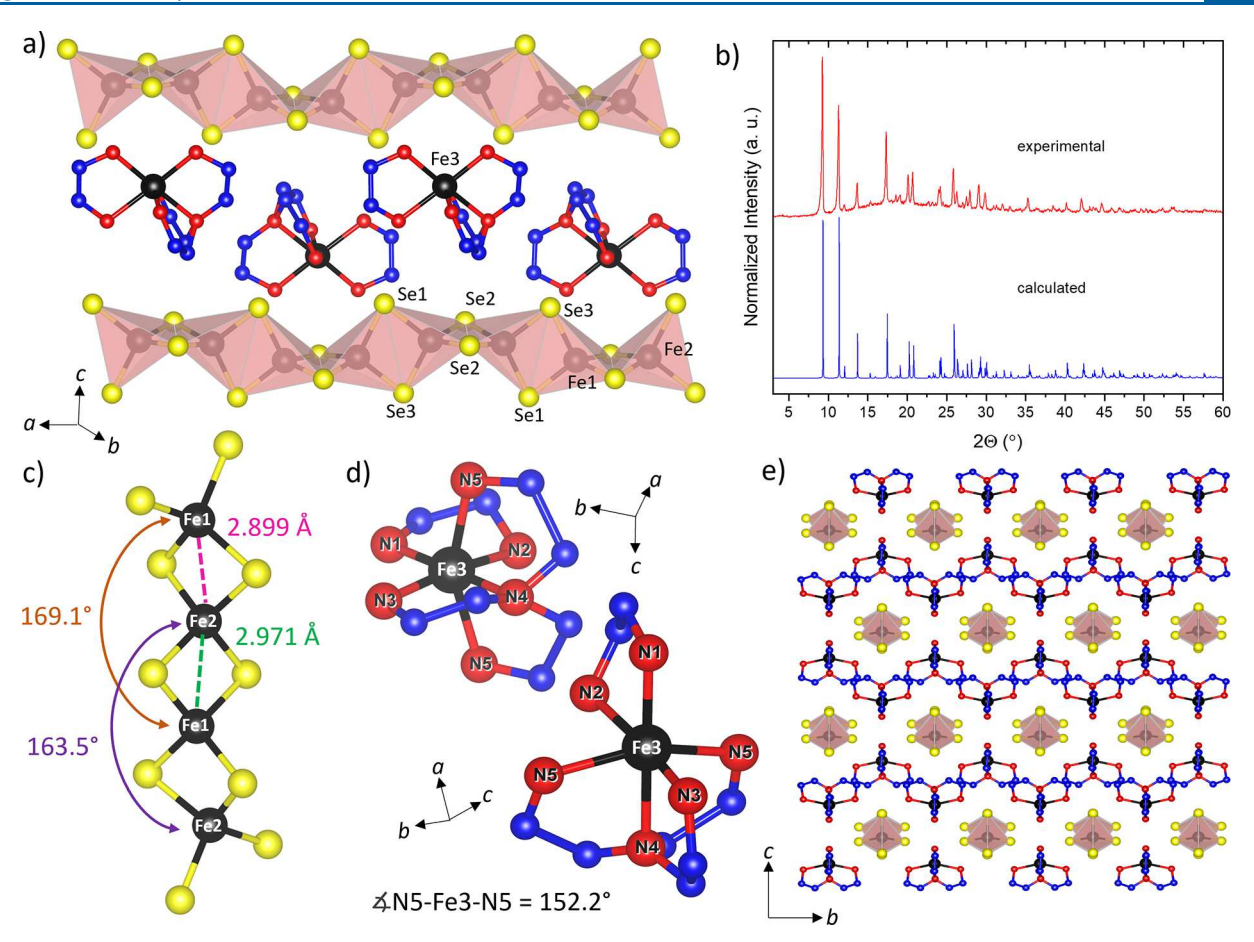


Figure 3. Crystal structure of $[Fe(en)(tren)][FeSe_2]_2$. (a) Enlarged view of $FeSe_2$ chains and $[Fe(en)(tren)]^{2+}$ complexes visualized along [111] direction; (b) Comparison of calculated and experimental powder X-ray diffraction patterns; (c) Detailed structure of the 1D $FeSe_2$ chain indicting bond distances and angles; (d) Detailed views of the distorted $[Fe(en)(tren)]^{2+}$ complex; (e) General view along [100]. Fe: black, Se: yellow, N: red, C: blue; H atoms of the ligands have been omitted for clarity. Note that the disorder of C and N atoms is not shown for clarity.

Table 2. Comparison of Structural and Magnetic Properties in One-Dimensional FeSe₂ Chain Compounds Reported to Date

structure [ref]	∠Fe−Fe−Fe (°)	∠Fe−Se−Fe (°)	Fe-Fe distances (Å)	intrachain magnetic coupling and Weiss constant	interchain magnetic ordering
[Fe(tren)][FeSe2]220	157.68, 157.82	70.55-72.89	2.727, 2.797	FM, +145 K	AFM
[Fe(en) ₃] ₃ (FeSe ₂) ₄ Cl ₂ ²³	156.97, 160.90	73.98-76.64	2.904, 2.932	AFM, -11 K	Spinglass
[Fe(en)(tren)][FeSe ₂] ₂ [current work]	163.5, 169.1	75.34-76.33	2.899(2), 2.971(2)	FM, +54 K	AFM
$[Fe(en)_3][FeSe_2]_2^{22}$	164.41, 166.27	77.49-77.51	2.948, 2.969	AFM, -6.4 K	None
			2.981		
$[Fe(dien)_2][FeSe_2]_2^{20}$	169.16	75.23-75.31	2.910, 2.912	AFM, -5.2 K	None
$[Fe(en)_2][FeSe_2]_2^{21}$	176.41	74.99-76.22	2.869, 2.944	AFM, -105 K	AFM
KFeSe ₂ ⁷	177.00	73.02	2.82	AFM	AFM

The broad feature centered at $\sim 3450~\rm cm^{-1}$ is due to the O–H stretching modes of the surface adsorbed water. A broad multiplet of peaks appearing in the 3300–3050 cm⁻¹ region is attributed to the N–H stretching vibrations while the doublet around $\sim 2850~\rm cm^{-1}$ represents C–H stretching modes. The sharp band at $\sim 1600~\rm cm^{-1}$ is assigned to the NH₂ bending modes followed by CH₂ bending and other deformational

modes in the $1500-1400~\rm cm^{-1}$ region. CH_2/NH_2 twisting and wagging modes lie in the $1400-1300~\rm cm^{-1}$ region. The bands at $1100-950~\rm cm^{-1}$ belong to the C–C and C–N skeletal vibrations with a clearly resolved asymmetric doublet associated with the stretching modes of the tertiary amine group of *tren*. NH_2 rocking modes are assigned to the bands appearing between $850~\rm and~700~cm^{-1}$. Finally, the Fe–N

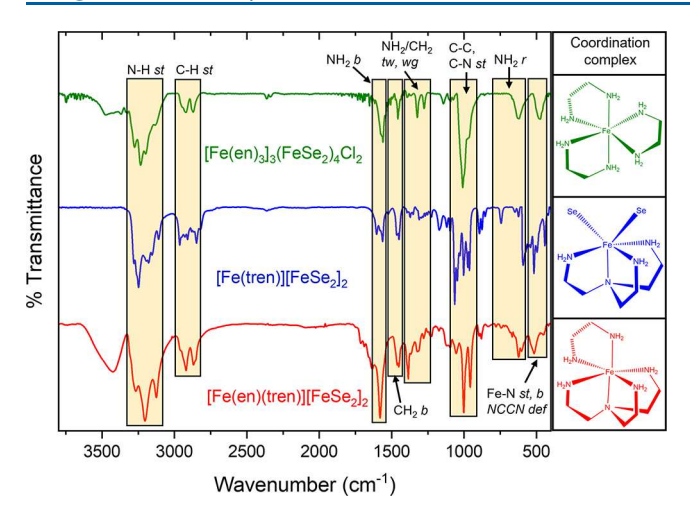


Figure 4. FTIR spectra of [Fe(en)(tren)][FeSe₂]₂, [Fe(tren)][FeSe₂]₂, and [Fe(en)₃]₃(FeSe₂)₄Cl₂ with the band assignments shown in yellow boxes. Schematics of the coordination complexes in each compound are given in the left column. *st*: stretching; *b*:bending; *tw*: twisting; *wg*: wagging; *r*: rocking; *def*: ring deformations.

stretching vibrations, N–Fe–N bending modes, and N–C–C-N ring deformations are characterized by multiple bands from 600 to 450 cm $^{-1}$. IR bands for Fe–Se vibrational modes are expected to be below 400 cm $^{-1}$ which is outside of the measured range. Overall, the main features and the regions where bands appear are comparable in all three spectra. However, the $[Fe(en)(tren)][FeSe_2]_2$ spectrum is not a simple superposition of the peaks in $[Fe(en)_3]_3(FeSe_2)_4Cl_2$ and $[Fe(tren)][FeSe_2]_2$ spectra. Differences in the structure of the bands are a consequence of the discrepancies in coordination, distortion, orientation, and hydrogen bonding networks of the participating $-NH_2$ groups in the Fe-amine complexes.

Magnetism. Temperature dependence of magnetic susceptibility (χ) for [Fe(en)(tren)][FeSe₂]₂ shows a clear upturn and a peak below 20 K, indicating bulk AFM ordering. The maximum value of χ is achieved at the ordering temperature, $T_{\rm N}=4$ K (the blue curves in Figure 5a,c). Curie—Weiss fitting of the inverse susceptibility data between 175 and 300 K (black line in Figure 5b) results in C=2.44(1) emu K mol⁻¹, which corresponds to an effective magnetic moment $\mu_{\rm eff}=4.42(1)$ $\mu_{\rm B}$ per formula unit. The higher covalency of Fe—Se bonds (as compared to Fe—O bonds) leads to partial quenching of the

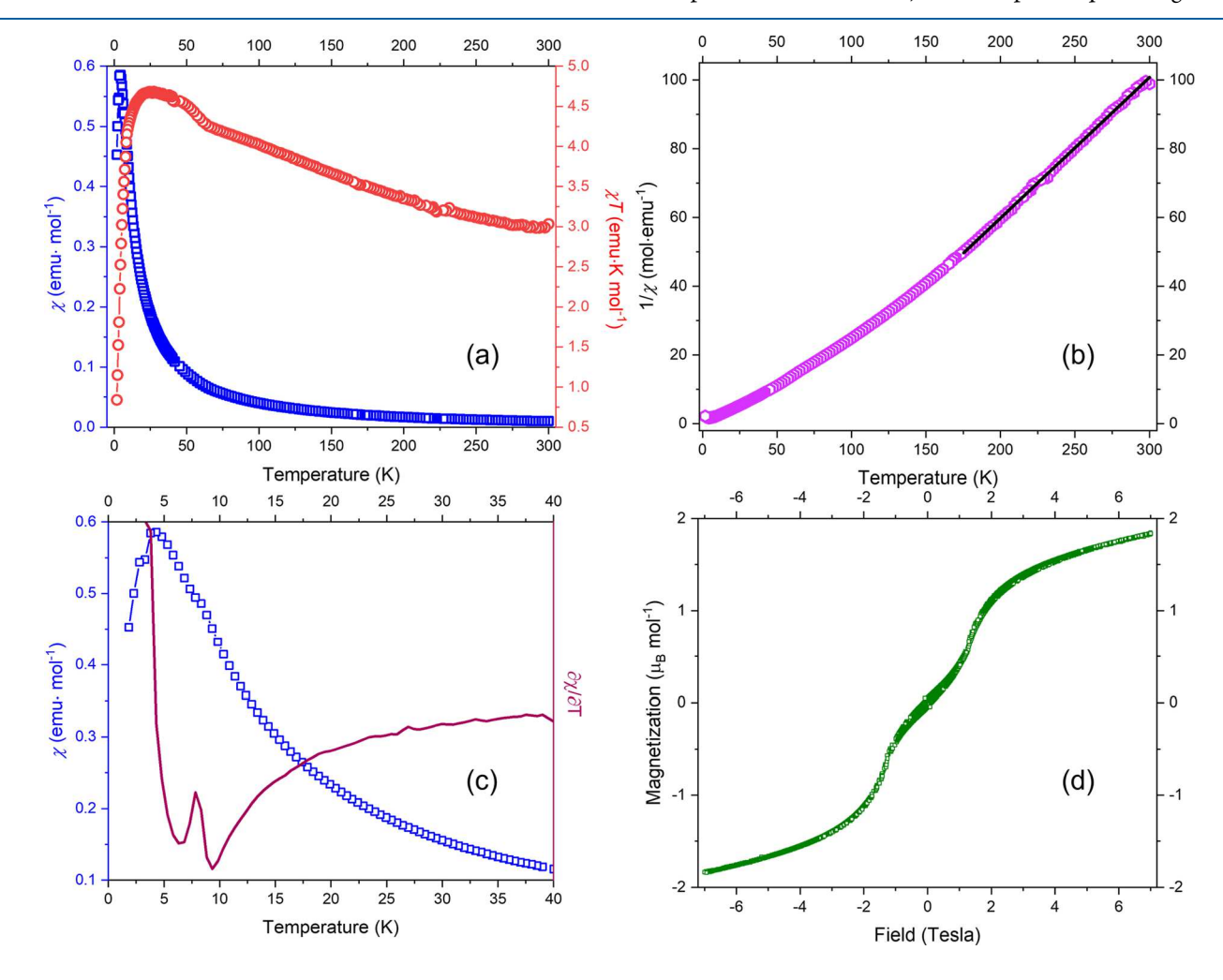


Figure 5. Magnetic measurements for $[Fe(en)(tren)][FeSe_2]_2$ under an applied field of 1000 Oe. (a) χ vs T (blue squares) and χT vs T (red circles) curves; (b) $1/\chi$ vs T curve with the Curie–Weiss fit in the 175–300 K range (R^2 = 0.99932) given in a solid black line; (c) χ vs T curve below 40 K emphasizing the low temperature features (blue squares) and the derivative of χ with respect to temperature (Fisher heat capacity) indicating two different events below 10 K (magenta line); (d) Isothermal field dependence of magnetization measured at 2 K.

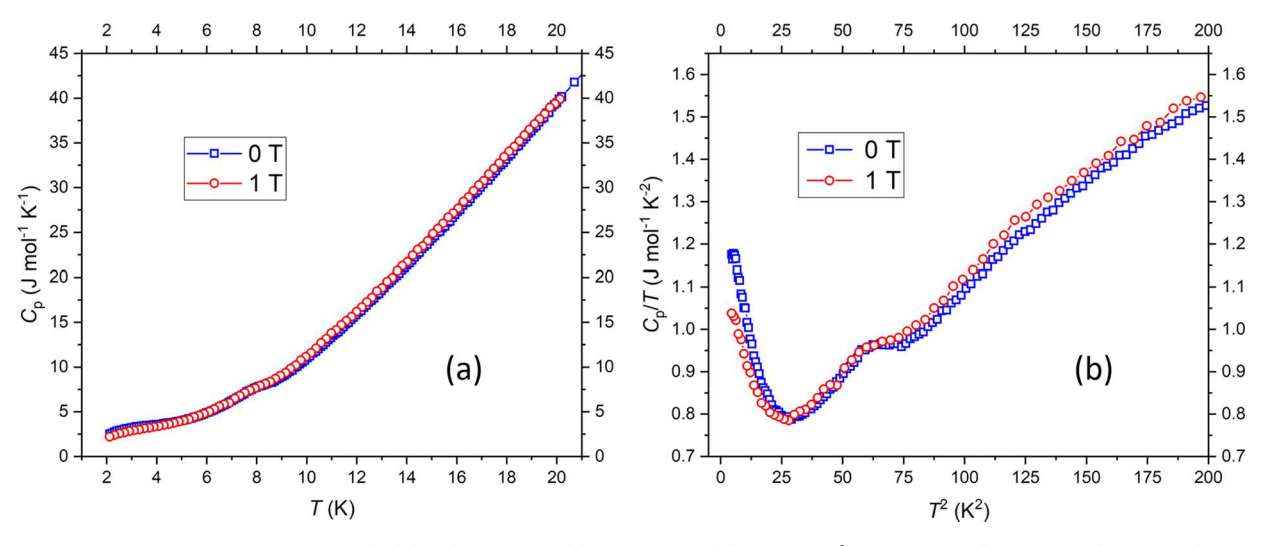


Figure 6. Electron heat capacity data for $[Fe(en)(tren)][FeSe_2]_2$. (a) C_p vs T and (b) C_p/T vs T^2 curves at 0 T (blue squares) and 1 T (red circles) applied magnetic field.

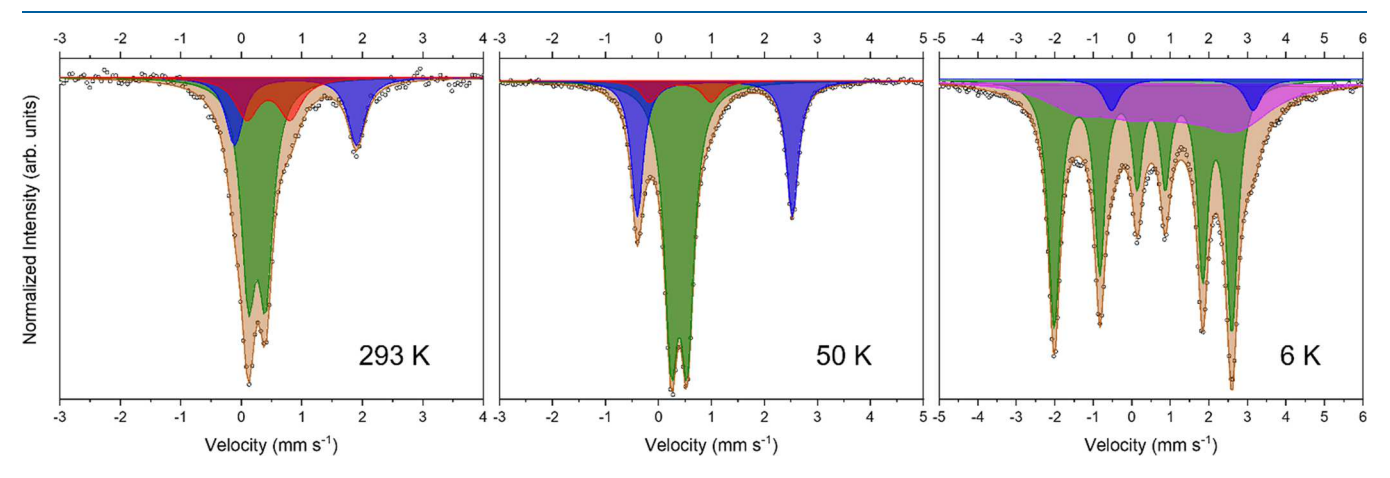


Figure 7. 57 Fe Mössbauer spectra for the $[Fe(en)(tren)][FeSe_2]_2$ sample measured at various temperatures. Experimental: black circles; total calculated: brown; Fe^{3+} : green; nonmagnetic Fe^{2+} : blue; magnetic Fe^{2+} : magenta; admixture: red.

magnetic moment in 3d metal chalcogenides, 52,53 hence, observation of a reduced magnetic moment for Fe atoms in the Fe-Se chains is common for chain compounds such as [Fe(en)₃][FeSe₂]₂, ²² [Fe(tren)][FeSe₂]₂, ²⁰ and [Fe(en)₃]₃(FeSe₂)₄Cl₂. ²³ A positive Weiss constant, $\theta =$ +53.8(6) K, obtained from the Curie-Weiss fit, and the upward trend in the χT value with decreasing temperature (the red curve in Figure 5a) indicate FM nearest-neighbor interactions in the FeSe2 chains, but not as strong as reported for [Fe(tren)][FeSe₂]₂ ($\theta = +145 \text{ K}$), which can be explained by the stronger chain deformation and shorter Fe-Fe distances in the latter compound (Table 2). When magnetic measurements were repeated on a freshly synthesized sample, the lowtemperature inflection point was reproduced for 1000 Oe (Figure S3). Increasing the applied field to 3 T resulted in the suppression of the AFM ordering within the accessible temperature range, with no FM-type feature observed in the temperature dependence of χ (Figures S4 and S5).

A closer examination of the low-temperature region of magnetic susceptibility reveals an additional kink around 10 K. The derivative of the magnetic susceptibility with respect to temperature supports the presence of two low-temperature anomalies (Figure 5c). It is possible that the AFM ordering takes place in two steps, with a slight reorientation of magnetic

moments. A conclusive answer to this question can be obtained by magnetic structure determination from neutron diffraction, which is challenging due to the high content of hydrogen atoms and the high cost of deuterated amines.

The isothermal field-dependent magnetization measured at 2 K shows a spin reorientation transition at 1.5 T (Figure 5d) which manifests into a distorted S-shaped behavior at higher temperatures (Figure S6). Similar behavior was also observed for other 1D chain compounds with FM *intra*-chain and AFM *inter*-chain interactions. However, despite the spin reorientation transition taking place \sim 1.5 T at base temperature, no ferromagnetic ordering was observed in χ vs T measurements at the 3 T applied field. This may indicate that the magnetic state of the title compound after the spin-reorientation transition is not ferro but rather ferrimagnetic. This hypothesis is supported by the maximum magnetization of 1.84 $\mu_{\rm B}$ achieved at 7 T which is significantly lower than the maximum magnetization of 3.25 $\mu_{\rm B}$ reported for $[{\rm Fe}({\rm tren})][{\rm FeSe}_2]_2$.

Heat Capacity. Heat capacity (C_p) measurements were conducted on a cold-pressed pellet under 0 and 1 T applied magnetic fields. The C_p vs T curve under zero field shows broad cusps at 7–8.5 K and 3–4 K (Figure 6a) which agrees with the anomalies seen in the temperature dependence of

magnetic susceptibility (Figure 5a). When a 1 T magnetic field is applied, no substantial changes are observed, but the intensity of the low-temperature cusp, 3–4 K, is suppressed. The $C_{\rm p}/T$ vs T^2 plots below T^2 < 200 K, enhances the peak at $T^2 \sim 64$ K² supporting possible magnetic ordering event (Figure 6b).

⁵⁷Fe Mössbauer Spectroscopy. To investigate the oxidation states and magnetic properties of Fe^{chain} and $Fe^{complex}$ atoms, ⁵⁷Fe Mössbauer spectra of a $[Fe(en)(tren)][FeSe_2]_2$ sample were collected at 293, 50, and 6 K (Figure 7). At room temperature, the spectrum is best fitted using three strongly overlapping doublets with no magnetically split components (Table 3). The first doublet, Q_1 , with relatively low centroid

Table 3. Summary of Refined Mössbauer Parameters for $[Fe(en)(tren)][FeSe_2]_2$ Sample, Measured at 6, 50, and 293 K: Centroid Shift, Δ , Quadrupole Splitting/Quadrupole Shift, $\Delta E_Q/\varepsilon$, Magnetic Hyperfine Field, B_{hf} , Full-Width at Half Maximum, Γ , and Intensity, I, of the Different Components, Q^a

components	parameters	6 K	50 K	293 K
Q_1 : T_d Fe ³⁺	$\delta \; (\text{mm/s})$	0.40	0.39	0.26
	ΔE_Q or ε (mm/s)	-0.11	0.30	0.29
	$B_{\rm hf}$ (T)	14.3		
	Γ (T)	0.32	0.31	0.29
	I (%)	60	63	58
Q_2 : O_h Fe ²⁺ (nonmagnetic)	$\delta \ (\text{mm/s})$	1.31	1.07	0.90
	$\Delta E_Q \left(mm/s\right)$	3.67	2.93	2.02
	Γ (mm/s)	0.50	0.27	0.34
	I (%)	5	30	24
Q _{2A} : O _h Fe ²⁺ (magnetic)	$\delta (\text{mm/s})$	1.01		
	$\varepsilon \; (\text{mm/s})$	-0.24		
	$B_{ m hf}$ (T)	13.4		
	Γ (T)	1.81		
	I (%)	35		
Q ₃ : admixture	$\delta \ (\text{mm/s}) \ \Delta E_{ ext{Q}} \ (\text{mm/s}) \ \Gamma \ (ext{T})$		0.42 1.16 0.40	0.45 0.71 0.46
	I (1) I (%)		7	18
	1 (70)		/	10

^aEstimated Errors: I ± 2%, δ , Δ E $_{\rm Q}$, and ε ± 0.001 mm/s, $B_{\rm hf}$ ± 0.2 T, and Γ ± 0.05 mm/s.

shift, δ , and quadrupole splitting, ΔE_{Q_2} values of 0.26 and 0.29 mm/s respectively, are characteristic for tetrahedrally coordinated Fe³+ ions in the 1D-FeSe₂ sublattice. These values are slightly different to what was reported for tetrahedral Fe³+ in [Fe(tren)][FeSe₂]₂ (δ = 0.34 mm/s, ΔE_Q = 0.41 mm/s)²0 and [Fe(en)₃]₃(FeSe₂)₄Cl₂ (δ = 0.26 mm/s, ΔE_Q = 0.35 mm/s).²³ In general, in iron chalcogenides, the presence of metal—metal bonding may significantly affect the Mössbauer parameters. The second doublet, Q_2 , of δ = 0.90 mm/s and much larger ΔE_Q = 2.01 mm/s, corresponds to high-spin Fe²+ ions in the [Fe(en)(tren)]²+ complex. The high quadrupole splitting parameter is larger than the values observed at room temperature for more symmetric [Fe(en)₃]²+ complexes in [Fe(en)₃]₃(FeSe₂)₄Cl₂ (ΔE_Q = 0.60 mm/s)²³ and Fe₂As₃Se₁₂(en)₆(H₂O) (ΔE_Q = 0.70 mm/s).²⁴ Increase in quadrupole splitting is due to the asymmetry around the Fe²+

ions surrounded by two different sterically strained *en* and *tren* ligands. The ratio between the intensities of Q_1 : Q_2 is approximately 2:1, which further confirms the separation of Fe³⁺ and Fe²⁺ sublattices predicted by the charge balance and bond valence sum counting. Apart from this, another component represented by the red doublet, Q_3 , having intermediate δ and ΔE_Q values, is believed to be an amorphous admixture not detected by PXRD. The contribution of the admixture to the Mössbauer spectra reduces with temperature due to variation of the recoil-less fraction such that it was not detectable for the base temperature spectrum.

At 50 K, the spectrum can be fitted with the same three components but with increased centroid shifts due to a secondorder Doppler effect. Quadrupole splitting of the amine complex increases, a common observation on hybrid Fe-Seamine compounds. At 6 K, the spectrum can be fitted with two magnetic sextets and one nonmagnetic doublet. The Q_1 component representing Fe3+ in the tetrahedral chains completely transforms into a sextet with a magnetic hyperfine field of 14.3 T indicating a fully magnetically ordered state in the Fe-Se chains. The Fe²⁺ sublattice is represented by two signals here. A smaller fraction, 1/8, of Fe2+ is represented by Q_2 nonmagnetic doublet with a δ of 1.31 mm/s and a ΔE_O of 3.67 mm/s, which are characteristic values for high-spin Fe²⁺ in an asymmetric environment at low temperature. The rest of the Fe2+ signal can be described as Q2A, which is a broad magnetic sextet. An increase in the overall intensity of Fe²⁺ subspectra upon cooling is a consequence of the recoil-less fraction for Fe²⁺ being temperature sensitive.²³ The intensity of the Q₃ component decreases with temperature, and this component was omitted upon fitting the base temperature spectrum to avoid overparameterization.

Partial hyperfine splitting of the amine complex Fe^{2+} signal was previously observed for $[Fe(en)_2][FeSe_2]_2$ and $[Fe(tren)][FeSe_2]_2$. $[Fe(tren)][FeSe_2]_2^{20}$ exhibits long-range AFM ordering at high temperatures, a positive Weiss constant $(\theta = +145 \text{ K})$ and a larger hyperfine field (27.6 T), while $[Fe(en)_2][FeSe_2]_2^{21}$ with AFM *intra*chain interactions exhibit much weaker (5.9 T) induced hyperfine splitting of Fe^{2+} . However, in both cases, the magnetic exchange is facilitated via respective *cis*-Fe(tren)Se₂ and *trans*-Fe(en)₂Se₂ fragments that make covalent connections between the Fe-*amine* complex and the 1D FeSe₂ chains. Therefore, $[Fe(en)(tren)][FeSe_2]_2$ is an important example of achieving 3D magnetic ordering by noncovalent hydrogen bonding interactions.

DFT Calculations. DFT calculations were performed on a simplified model by replacing $[Fe(en)(tren)]^{2+}$ complexes with Ba²⁺ ions, adopting a charge-neutral unit cell: Ba₄Fe₈Se₁₆. Such a model contains two parallel [Fe₄Se₈] chains. The total energy calculations with several spin configurations show that the AFM-type interaction between the nearest neighbors is highly favorable, as evident from the lowest energy spin configurations 3 and 4 in Table S1 and Figure 8. Spin configurations with FM intrachain interactions were computed to have significantly higher energy, while ferrimagnetic chains have intermediate energies. To determine the nature of the intrachain interactions, linear response calculations were conducted to obtain exchange constants for all pairwise interactions. The exchange constant calculations reveal strong AFM interactions between nearest-neighbor atoms (large positive values of 43-47 meV) and are consistent with the total energy calculations (Table S2). Additionally, the calculations indicate noteworthy AFM interactions between

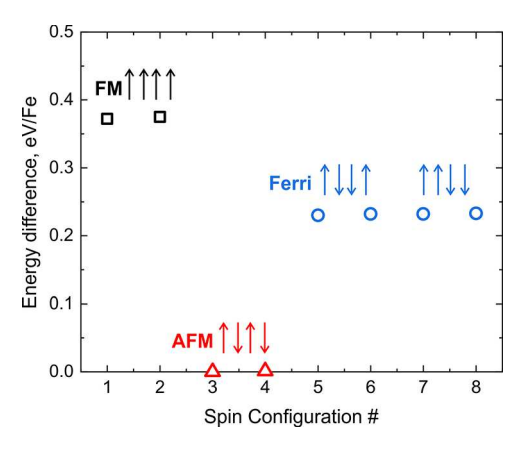


Figure 8. Total energy difference for different spin configurations (SC) for various *intra*chain and *inter*chain interactions in the simplified $Ba_4Fe_8Se_{16}$ model. The numerical data are shown in Table S1.

second-nearest neighbors (~4 meV). However, due to the competing interactions with the immediate neighbors, the AFM interactions between the second-nearest neighbors are obscured. Overall, the calculations support an AFM ordering at low temperatures and suggest strong *intra*chain AFM but much weaker *inter*chain FM (small negative values) exchange coupling.

The calculations did not capture the reason for the positive Weiss constant and the observed upturn of χ vs T temperature dependence, both of which indicated some kind of ferromagnetic nearest-neighbor interactions. We believe Se… H hydrogen bonding interactions between the heteroleptic complex and the Fe–Se chains at finite temperature combined with a disorder in the ligand positions may affect the *intra*chain interactions favoring ferrimagnetic chains such as spin configurations 5–8 in Table S1 and Figure 8. Modeling the system with an explicit spin Hamiltonian will be very challenging, given the extended nature of the system and the complexity of disordered $[Fe(en)(tren)]^{2+}$ moieties.

Given the broad nature of the magnetic sextet for Fe²⁺ in the Mössbauer spectrum at base temperature and the results of magnetization, heat capacity, and DFT studies, one can summarize the magnetic properties for [Fe(en)(tren)][FeSe₂]₂ as following: at elevated temperatures in the chains there are competing FM and AFM Fe³⁺-Fe³⁺ interactions. Upon cooling below 10 K, in two subsequent events, AFM ordering in the chains is achieved at 4 K in line with 0 K DFT calculations. The generated internal magnetic field affects the Fe²⁺-amine sublattice resulting in a broad ⁵⁷Fe Mössbauer signal. The incomplete hyperfine splitting of the Fe^{2+} signal may be due to the variation of local magnetic moments surrounding Fe³⁺ due to weak interchain coupling or due to disorder in Fe(tren)(en) complex resulting in variation in N-H...Se hydrogen bonding. We hypothesize that under an applied magnetic field, the AFM chains are converted into ferrimagnetic chains, yet complete FM chains are not achieved even at a 7 T field as evidenced from the reduced magnetic moment.

CONCLUSIONS

A novel mixed-valent chain compound [Fe(en)(tren)]-[FeSe₂]₂ has been synthesized by a solvothermal method using a combination of *en* and *tren* as both ligands and solvents. Asymmetric [Fe(en)(tren)]²⁺ complexes residing between tetrahedral FeSe₂ chains result in chain distortion with alternating Fe^{chain}—Fe^{chain} distances facilitating ferrimagnetic exchange in the chains. Magnetic, ⁵⁷Fe Mössbauer spectroscopy, and heat capacity studies reveal two magnetic ordering events happening below 10 K. DFT calculations indicate that complete AFM ordering in the chains takes place at the base temperature. Current work demonstrates that heteroleptic Fe(II) complexes can be used to impact the properties of hybrid materials by providing different interactions due to the asymmetric shape of the complex incorporated into the interchain space. Further explorations of Fe coordination chemistry aimed at varying ligand fields are currently underway.

ASSOCIATED CONTENT

Supporting Information

The Supporting Information is available free of charge at https://pubs.acs.org/doi/10.1021/acs.inorgchem.3c03440.

Tables with a summary of DFT calculations; crystallographic file; additional structural, powder X-ray diffraction; and magnetic measurements figure (PDF)

Accession Codes

CCDC 2202574 contains the supplementary crystallographic data for this paper. These data can be obtained free of charge via www.ccdc.cam.ac.uk/data_request/cif, or by emailing data_request@ccdc.cam.ac.uk, or by contacting The Cambridge Crystallographic Data Centre, 12 Union Road, Cambridge CB2 1EZ, UK; fax: +44 1223 336033.

AUTHOR INFORMATION

Corresponding Author

Kirill Kovnir — Department of Chemistry, Iowa State University, Ames, Iowa 50011, United States; U.S. Department of Energy, Ames National Laboratory, Ames, Iowa 50011, United States; ⊚ orcid.org/0000-0003-1152-1912; Email: kovnir@iastate.edu

Authors

Eranga H. Gamage — Department of Chemistry, Iowa State University, Ames, Iowa 50011, United States; U.S. Department of Energy, Ames National Laboratory, Ames, Iowa 50011, United States; orcid.org/0000-0002-6954-7130

Saeed Kamali – Mechanical, Aerospace & Biomedical Engineering Department, University of Tennessee Space Institute, Tullahoma, Tennessee 37388, United States; Department of Physics and Astronomy, Middle Tennessee State University, Murfreesboro, Tennessee 37132, United States

Govind Sasi Kumar – Department of Chemistry and Biochemistry, Florida State University, Tallahassee, Florida 32306, United States

Judith K. Clark – Department of Chemistry and Biochemistry, Florida State University, Tallahassee, Florida 32306, United States

Yongbin Lee – U.S. Department of Energy, Ames National Laboratory, Ames, Iowa 50011, United States

Yao Abusa – Department of Chemistry, Iowa State University, Ames, Iowa 50011, United States; orcid.org/0000-0003-2508-5330

Philip Yox — Department of Chemistry, Iowa State University, Ames, Iowa 50011, United States; U.S. Department of Energy, Ames National Laboratory, Ames, Iowa 50011, United States; orcid.org/0000-0002-8524-8202

Liqin Ke — U.S. Department of Energy, Ames National Laboratory, Ames, Iowa 50011, United States

Michael Shatruk — Department of Chemistry and Biochemistry, Florida State University, Tallahassee, Florida 32306, United States; National High Magnetic Field Laboratory, Tallahassee, Florida 32310, United States; orcid.org/0000-0002-2883-4694

Complete contact information is available at: https://pubs.acs.org/10.1021/acs.inorgchem.3c03440

Author Contributions

The manuscript was written through contributions of all authors.

Funding

This research was supported by the National Science Foundation DMR-2003783 grant to K.K. Magnetic characterization performed by J.K.C., G.S.K., and M.S. were supported by NSF DMR-1905499. NSF's ChemMatCARS Sector 15 is supported by the Divisions of Chemistry (CHE) and Materials Research (DMR), National Science Foundation, under grant number NSF/CHE-1834750. Use of the Advanced Photon Source, an Office of Science User Facility operated for the U.S. Department of Energy (DOE) Office of Science by Argonne National Laboratory, was supported by the U.S. DOE under Contract No. DE-AC02-06CH11357. Y.L. and L.K. were supported by the U.S. Department of Energy, Office of Science, Office of Basic Energy Sciences, Materials Sciences and Engineering Division. Ames National Laboratory is operated for the U.S. Department of Energy by Iowa State University under Contract No. DE-AC02-07CH11358.

Notes

The authors declare no competing financial interest.

ACKNOWLEDGMENTS

We are thankful to Dr. Arkady Ellern for helping with the crystal structure solution and Gayatri Viswanathan for EDS/SEM data collection. We are also thankful to synchrotron scientists Prof. Yu-Sheng Chen and Tieyan Chang of ChemMatCARS, University of Chicago, for their help in arranging the remote single crystal diffraction experiments and for single crystal data collection on our behalf and Dr. Wenqian Xu and Dr. Andrey Yakovenko for their help with collecting *in situ* synchrotron XRD data.

REFERENCES

- (1) Takano, M.; Azuma, M.; Hiroi, Z.; Bando, Y.; Takeda, Y. Superconductivity in the Ba-Sr-Cu-O System. *Phys. C Supercond.* **1991**, *176*, 441–444.
- (2) Goodenough, J. B.; Manthiram, A. Crystal Chemistry and Superconductivity of the Copper Oxides. *J. Solid State Chem.* **1990**, 88, 115–139.
- (3) Kamihara, Y.; Watanabe, T.; Hirano, M.; Hosono, H. Iron-Based Layered Superconductor $La[O_{1-x}F_x]$ FeAs (x = 0.05-0.12) with $T_c = 26$ K. J. Am. Chem. Soc. **2008**, 130, 3296–3297.
- (4) Hosono, H.; Yamamoto, A.; Hiramatsu, H.; Ma, Y. Recent Advances in Iron-Based Superconductors toward Applications. *Mater. Today* **2018**, *21*, 278–302.

- (5) Zhao, X.; Ma, F.; Lu, Z.-Y.; Xiang, T. AFeSe₂ (A = Tl, K, Rb, or Cs): Iron-Based Superconducting Analog of the Cuprates. *Phys. Rev. B* **2020**, *101*, No. 184504.
- (6) Stüble, P.; Röhr, C. Cs[FeSe₂], Cs₃[FeSe₂]₂, and Cs₇[Fe₄Se₈]: Missing Links of Known Chalcogenido Ferrate Series. *Z. anorg. allg. Chem.* **2017**, *643*, 1462–1473.
- (7) Bronger, W.; Kyas, A.; Müller, P. The Antiferromagnetic Structures of KFeS₂, RbFeS₂, KFeSe₂, and RbFeSe₂ and the Correlation between Magnetic Moments and Crystal Field Calculations. *J. Solid State Chem.* **1987**, *70*, 262–270.
- (8) Klepp, K.; Boller, H. Die Kristallstruktur von TlFeSe₂ Und TlFeS₂. Monat. Chem. **1979**, 110, 1045–1055.
- (9) Bronger, W.; Ruschewitz, U.; Müller, P. New Ternary Iron Sulphides A_3 Fe₂S₄ (A = K, Rb, Cs): Syntheses and Crystal Structures. *J. Alloys Compd.* **1995**, 218, 22–27.
- (10) Schwarz, M.; Stüble, P.; Köhler, K.; Röhr, C. New Mixed-Valent Alkali Chain Sulfido Ferrates $A_{1+x}[\text{FeS}_2]$ (A = K, Rb, Cs; x = 0.333-0.787). Z. Kristallogr. **2020**, 235, 275–290.
- (11) Vivanco, H. K.; Rodriguez, E. E. The Intercalation Chemistry of Layered Iron Chalcogenide Superconductors. *J. Solid State Chem.* **2016**, 242, 3–21.
- (12) Krzton-Maziopa, A.; Pesko, E.; Puzniak, R. Superconducting Selenides Intercalated with Organic Molecules: Synthesis, Crystal Structure, Electric and Magnetic Properties, Superconducting Properties, and Phase Separation in Iron Based-Chalcogenides and Hybrid Organic-Inorganic Superconductors. *J. Phys.: Condens. Matter* **2018**, 30, 243001.
- (13) Hayashi, F.; Lei, H.; Guo, J.; Hosono, H. Modulation Effect of Interlayer Spacing on the Superconductivity of Electron-Doped FeSe-Based Intercalates. *Inorg. Chem.* **2015**, *54*, 3346–3351.
- (14) Shi, M. Z.; Wang, N. Z.; Lei, B.; Shang, C.; Meng, F. B.; Ma, L. K.; Zhang, F. X.; Kuang, D. Z.; Chen, X. H. Organic-Ion-Intercalated FeSe-Based Superconductors. *Phys. Rev. Mater.* **2018**, *2*, No. 074801.
- (15) Krzton-Maziopa, A.; Pomjakushina, E. V.; Pomjakushin, V. Y.; Von Rohr, F.; Schilling, A.; Conder, K. Synthesis of a New Alkali Metal—Organic Solvent Intercalated Iron Selenide Superconductor with $T_c \approx 45$ K. J. Phys.: Condens. Matter **2012**, 24, No. 382202.
- (16) Krzton-Maziopa, A. Intercalated Iron Chalcogenides: Phase Separation Phenomena and Superconducting Properties. *Front. Chem.* **2021**, *9*, No. 640361.
- (17) Wu, M.; Rhee, J.; Emge, T. J.; Yao, H.; Cheng, J. H.; Thiagarajan, S.; Croft, M.; Yang, R.; Li, J. A Low Band Gap Iron Sulfide Hybrid Semiconductor with Unique 2D $\left[\text{Fe}_{16}\text{S}_{20}\right]^{8}$ Layer and Reduced Thermal Conductivity. *Chem. Commun.* **2010**, *46*, 1649–1651.
- (18) Harmer, C.; Pak, C.; Greenfield, J.; Adeyemi, A.; Gamage, E.; Kovnir, K. Non-Innocent Intercalation of Diamines into Tetragonal FeS Superconductor. *ACS Appl. Energy Mater.* **2021**, *4*, 42–46.
- (19) Harmer, C. P.; Kamali, S.; Lebedev, O. I.; Lee, S. J.; Ribeiro, R. A.; Canfield, P. C.; Kovnir, K. Pseudo-Polymorphism in Layered FeS Intercalates: A Competition between Charged and Neutral Guest Species. *Chem. Mater.* **2022**, *34*, 5397–5408.
- (20) Greenfield, J. T.; Pak, C.; Kamali, S.; Lee, K.; Kovnir, K. Control over Connectivity and Magnetism of Tetrahedral FeSe₂ Chains through Coordination Fe-Amine Complexes. *Chem. Commun.* **2015**, *51*, 5355–5358.
- (21) Pak, C.; Kamali, S.; Pham, J.; Lee, K.; Greenfield, J. T.; Kovnir, K. Chemical Excision of Tetrahedral FeSe₂ Chains from the Superconductor FeSe: Synthesis, Crystal Structure, and Magnetism of Fe₃Se₄(en)₂. *J. Am. Chem. Soc.* **2013**, *135*, 19111–19114.
- (22) Stahl, J.; Shlaen, E.; Singer, H.; Johrendt, D. Systematic Dimensional Reduction of the Layered β -FeSe Structure by Solvothermal Synthesis. *Dalt. Trans.* **2018**, *47*, 3264–3271.
- (23) Gamage, E. H.; Greenfield, J. T.; Unger, C.; Kamali, S.; Clark, J. K.; Harmer, C. P.; Luo, L.; Wang, J.; Shatruk, M.; Kovnir, K. Tuning Fe–Se Tetrahedral Frameworks by a Combination of [Fe(en)₃]²⁺ Cations and Cl⁻ Anions. *Inorg. Chem.* **2020**, *59*, 13353–13363.
- (24) Gamage, E. H.; Kamali, S.; Clark, J. K.; Lee, Y.; Yox, P.; Shafer, P.; Yaroslavtsev, A. A.; Ke, L.; Shatruk, M.; Kovnir, K. As-Se

- Pentagonal Linkers to Induce Chirality and Polarity in Mixed-Valent Fe—Se Tetrahedral Chains Resulting in Hidden Magnetic Ordering. *J. Am. Chem. Soc.* **2022**, *144*, 11283—11295.
- (25) Halcrow, M. A. The Effect of Ligand Design on Metal Ion Spin State-Lessons from Spin Crossover Complexes. *Crystals* **2016**, 6 (5), 58.
- (26) Garcia, Y.; Kahn, O.; Ader, J. P.; Buzdin, A.; Meurdesoif, Y.; Guillot, M. The Effect of a Magnetic Field on the Inversion Temperature of a Spin Crossover Compound Revisited. *Phys. Lett. A* **2000**, *271*, 145–154.
- (27) Ellermeier, J.; Stähler, R.; Bensch, W. Two New [Ni(Tren)₂]²⁺ Complexes: [Ni(Tren)₂]Cl₂ and [Ni(Tren)₂]WS₄. *Acta Crystallogr. C* **2002**, 58, m70–73.
- (28) Mosch-Zanetti, N. C.; Kopke, S.; Herbst-Irmer, R.; Hewitt, M. Unsymmetrical Tren-Based Ligands: Synthesis and Reactivity of Rhenium Complexes. *Inorg. Chem.* **2002**, *41*, 3513–3520.
- (29) Baral, M.; Gupta, A.; Akbar, R.; Kanungo, B. K. A Novel Tris(2-Aminoethyl)Amine Based Tripodal Ligand: Synthesis and Solution Coordination Studies with Trivalent Iron and Chromium. *J. Appl. Chem.* **2016**, 2016, No. 3757418.
- (30) Stock, P.; Wiedemann, D.; Petzold, H.; Hörner, G. Structural Dynamics of Spin Crossover in Iron(II) Complexes with Extended-Tripod Ligands. *Inorganics* **2017**, *5* (3), 60.
- (31) Hilbert, J.; Näther, C.; Weihrich, R.; Bensch, W. Room-Temperature Synthesis of Thiostannates from $\{[Ni(Tren)]_2[Sn_2S_6]\}$ -n. *Inorg. Chem.* **2016**, *55*, 7859–7865.
- (32) Behrens, M.; Scherb, S.; Näther, C.; Bensch, W. On the Incorporation of Transition Metal Atoms into Thiostannates: Synthesis, Crystal Structures and Spectroscopic Properties. *Z. anorg. allg. Chem.* **2003**, *629*, 1367–1373.
- (33) Lühmann, H.; Näther, C.; Bensch, W. Solvothermal Synthesis and Crystal Structure of the Non-Centrosymmetric Thioantimonate [Ni(Tren)₂]₂[Ni(Tren)(En)]₂(Sb₄S₈)₂·0.25H₂O. *Z. anorg. allg. Chem.* **2011**, *637*, 1007–1012.
- (34) Brar, A. S.; Kaur, S. Tetramethylguanidino-Tris(2-Aminoethyl)-Amine: A Novel Ligand for Copper-Based Atom Transfer Radical Polymerization. *J. Polym. Sci., Part A* **2005**, 43, 5906–5922.
- (35) Sheldrick, G. M. Crystal Structure Refinement with SHELXL. Acta Crystallogr. C 2015, 71 (Md), 3-8.
- (36) Sheldrick, G. M. A Short History of SHELX. *Acta Crystallogr. A* **2008**, *64*, 112–122.
- (37) Lagarec, K.; Rancourt, D. G. Recoil, Mössbauer Spectral Analysis Software for Windows; Department of Physics, University of Ottawa: Ottawa, 1998; 43.
- (38) Kresse, G.; Joubert, D. From Ultrasoft Pseudopotentials to the Projector Augmented-Wave Method. *Phys. Rev. B* **1999**, *59*, 1758.
- (39) Kresse, G.; Furthmüller, J. Efficient Iterative Schemes for *Ab Initio* Total-Energy Calculations Using a Plane-Wave Basis Set. *Phys. Rev. B* **1996**, *54*, 11169.
- (40) Kresse, G.; Furthmüller, J. Efficiency of Ab-Initio Total Energy Calculations for Metals and Semiconductors Using a Plane-Wave Basis Set. *Comput. Mater. Sci.* **1996**, *6*, 15–50.
- (41) Perdew, J. P.; Burke, K.; Ernzerhof, M. Generalized Gradient Approximation Made Simple. *Phys. Rev. Lett.* **1996**, 77, 3865.
- (42) Ke, L. Intersublattice Magnetocrystalline Anisotropy Using a Realistic Tight-Binding Method Based on Maximally Localized Wannier Functions. *Phys. Rev. B* **2019**, *99*, No. 054418.
- (43) Marzari, N.; Vanderbilt, D. Maximally Localized Generalized Wannier Functions for Composite Energy Bands. *Phys. Rev. B* **1997**, 56, 12847–12865.
- (44) Mostofi, A. A.; Yates, J. R.; Pizzi, G.; Lee, Y. S.; Souza, I.; Vanderbilt, D.; Marzari, N. An Updated Version of Wannier90: A Tool for Obtaining Maximally-Localised Wannier Functions. *Comput. Phys. Commun.* **2014**, *185*, 2309–2310.
- (45) Souza, I.; Marzari, N.; Vanderbilt, D. Maximally Localized Wannier Functions for Entangled Energy Bands. *Phys. Rev. B* **2001**, 65, No. 035109.

- (46) Marzari, N.; Mostofi, A. A.; Yates, J. R.; Souza, I.; Vanderbilt, D. Maximally Localized Wannier Functions: Theory and Applications. *Rev. Mod. Phys.* **2012**, *84*, 1419–1475.
- (47) Phan, H. V.; Chakraborty, P.; Chen, M.; Calm, Y. M.; Kovnir, K.; Keniley, L. K.; Hoyt, J. M.; Knowles, E. S.; Besnard, C.; Meisel, M. W.; Hauser, A.; Achim, C.; Shatruk, M. Heteroleptic FeII Complexes of 2,2'-Biimidazole and Its Alkylated Derivatives: Spin-Crossover and Photomagnetic Behavior. *Chem.-Eur. J.* **2012**, *18*, 15805–15815.
- (48) Brese, N. E.; O'Keeffe, M. Bond-valence Parameters for Solids. *Acta Crystallogr. B* **1991**, *47*, 192–197.
- (49) Garthow, D.; Schmidtke, H. H. The Infrared Spectra and Conformational Geometric Isomers of Diethylenetriamine Analysis of Complexes. *Inorg. Chim. Acta* **1968**, 248, 357–362.
- (50) Kürkçüoğlu, G. S.; Yeşilel, O. Z.; Sayın, E.; Enönlü, E.; Şahin, O. Synthesis and Structural Analysis of Heteronuclear Hexacyanochromate(III) Complex with Tris(2-Aminoethyl)Amine), [Cd(Tren)(Htren)][Cr(CN)₆]·2H₂O. *J. Mol. Struct.* **2020**, 1219, No. 128462.
- (51) Kürkçüoğlu, G. S.; Yeşilel, O. Z.; Şahin, O.; Sayin, E.; Büyükgüngör, O. Dinuclear Zinc(II) Complex with Tris(2-Aminoethyl) Amine Ligand: Synthesis Structure and Properties. *Z. Kristallogr.* **2015**, 230, 407–412.
- (52) Stevensson, B.; Edén, M. Metadynamics Simulations of the PH-Dependent Adsorption of Phosphoserine and Citrate on Disordered Apatite Surfaces: What Interactions Govern the Molecular Binding? *J. Phys. Chem. C* **2021**, *125*, 11987–12003.
- (53) Clark, J. K.; Pak, C.; Cao, H.; Shatruk, M. Helimagnetism in MnBi₂Se₄ Driven by Spin-Frustrating Interactions Between Antiferromagnetic Chains. *Cryst.* **2021**, *11*, 242.
- (54) Greenfield, J. T.; Ovidiu Garlea, V.; Kamali, S.; Chen, M.; Kovnir, K. Synthesis, Crystal Growth, Structural and Magnetic Characterization of NH₄MCl₂(HCOO), *M*=(Fe, Co, Ni). *J. Solid State Chem.* **2016**, 236, 222–229.